AGU PUBLICATIONS

JGR

Journal of Geophysical Research: Oceans

RESEARCH ARTICLE

10.1002/2014JC010466

Special Section:

Early scientific results from the salinity measuring satellites Aquarius/SAC-D and SMOS

Key Points:

- Low spatiotemporal resolution Aquarius L3 maps poorly resolve CCRs
- A data fusion technique is used to fuse Aquarius with other satellite products
- Aquarius L4 product fused with SSH best resolves CCR SSS signature and evolution

Correspondence to:
M. Umbert,
mumbert@icm.csic.es

Citation:
Umbert, M., S. Guimbard, G. Lagerloef, L. Thompson, M. Portabella, J. Ballabrera-Poy, and A. Turiel (2015), Detecting the surface salinity signature of Gulf Stream cold-core rings in Aquarius synergistic products, *J. Geophys. Res. Oceans*, *120*, 859–874, doi:10.1002/2014JC010466.

Received 22 SEP 2014
Accepted 14 JAN 2015
Accepted article online 21 JAN 2015
Published online 12 FEB 2015

Detecting the surface salinity signature of Gulf Stream cold-core rings in Aquarius synergistic products

M. Umbert[1], S. Guimbard[1], G. Lagerloef[2], L. Thompson[3], M. Portabella[1], J. Ballabrera-Poy[1], and A. Turiel[1]

[1]Departament of Physical and Technological Oceanography, Institut de Ciències del Mar, CSIC, Barcelona, Spain, [2]Earth and Space Research, Seattle, Washington, USA, [3]School of Oceanography, University of Washington, Seattle, Washington, USA

Abstract New sea surface salinity (SSS) observations derived from satellite remote sensing platforms provide a comprehensive view of salt exchanges across boundary currents such as the Gulf Stream. The high resolution (45 km spatial resolution and 3 day repeat subcycle) of the Soil Moisture and Ocean Salinity (SMOS) observations allows detection (and tracking) of meander and ring structures of the Gulf Stream from SSS maps. These structures are, however, not resolved by the relatively lower resolution (100 km and 7 day repeat subcycle) of Aquarius observations. A recently developed fusion technique, based on singularity analysis, is applied in this study to reconstruct these mesoscale (from 100 km and 3 days) features in Aquarius-derived products. New quarter-degree SSS maps are obtained by fusing Aquarius data with three different geophysical templates: sea surface height (SSH) from AVISO, SSS from SMOS, and sea surface temperature (SST) from AVHRR. The proposed method exploits the theoretical correspondence among the singularity exponents of different maps of ocean-surface remotely sensed scalar fields. The analysis results over the year 2012 show that merging Aquarius with SSH data provides a series of negative salinity anomalies that better collocate with the position of the cyclonic eddies identified from sea level anomaly maps. This result is consistent with the hypothesis that this SLA derived cyclonic eddies in this area are indeed CCRs shed off the GS.

1. Introduction

The Gulf Stream (GS) is a large-scale, western boundary current which transports warm (26–29°C) water northward along the East Coast of North America. It leaves the coast near Cape Hatteras and heads into the North Atlantic Ocean. Between Cape Hatteras (75°W and 35°N) and the New England Seamounts (i.e., roughly east of 65°W and north of 37°N, Figure 1) strong horizontal density gradients extend throughout the water column. The GS plays a major role in the meridional transport of heat and salt across the North Atlantic Ocean acting as a barrier between the cold (10–18°C during Summer) and relatively fresh (salinities around 30–32 in the practical salinity scale) [*Lewis*, 1980] waters from the Labrador Current and the warm (23°C), salty (36), clear, and unproductive waters of the Sargasso Sea.

After leaving Cape Hatteras, the Gulf Stream forms large-amplitude meanders (180–380 km) [*Savidge*, 2004] fed by a combination of baroclinic and barotropic instabilities. The size of the meanders may become large enough to break off the stream and loop back onto themselves to form detached rings [*Saunders*, 1971; *Evans et al*., 1985], especially after the Gulf Stream crosses the New England Seamounts. Meanders that separate north of the stream axis become anti-cyclonic rings of Sargasso Sea warm water surrounded by the cold waters of the continental margin. Conversely, the meanders separating south of the stream axis become cyclonic rings of tropical water around a cold, nutrient-rich center [*Richardson*, 1983; *Tomczak and Godfrey*, 2003]. The diameter of the rings typically range from 100 to 400 km [*Parker*, 1971]. They may have a signature in temperature and velocity down to the ocean floor, at depths of more than 4000 m, and usually move westward when they detach from the Gulf Stream and eastward when attached [*Fuglister*, 1977; *Csanady*, 1979]. Thus, warm-core rings can bring significant amounts of warm tropical water to the continental slope and near-shelf seas north of the Gulf Stream. Similarly, cold-core rings bring cold, nutrient-rich shelf water, to the biologically barren Sargasso Sea waters [*Pingree et al*., 1979; *Chelton et al*., 2011].

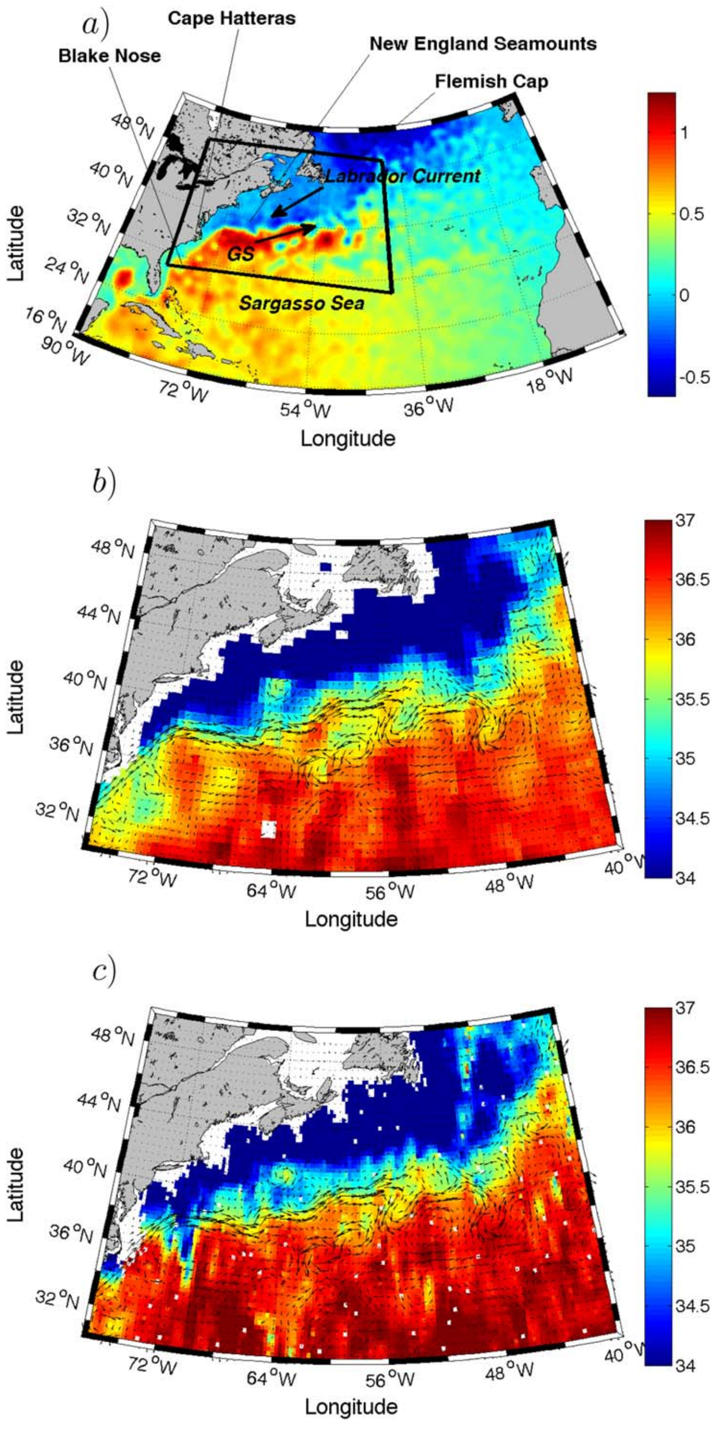

Figure 1. (a) Sea surface height map (m) for the 1 June 2012. Surface salinity maps corresponding to the 7 day averaged product centered on 1 June 2012 for (b) SMOS (0.25° resolution) and (c) Aquarius (0.25° resolution). The location of the Gulf Steam can be seen in the strong OSCAR currents indicated by the vectors.

Satellite detection of warm-core rings (WCRs) on the continental slope and near-shelf seas has frequently been reported and is well documented. As the surface temperature inside the ring is higher than the surrounding water, warm rings can be easily identified using infrared imagery and radar altimeters, and their monitoring is only limited by data missing due to clouds, aerosols, or orbital gaps. In this regard, sea surface height (SSH) is the only all season/all weather satellite product. But as SSH maps are constructed from altimetry tracks, they have limited temporal and spatial resolutions as compared with satellite imagery. Sea surface temperature (SST) imagery (excluding cloud areas) can be used to identify fronts, meanders, and/or eddies, although seasonal forcing of the mixed layer may mask the surface signatures. On the other hand, as warm rings are islands of nutrient-poor water in a nutrient-rich environment, they are also easily distinguished by ocean color images [*Cornillon et al*., 1994; *Leterme and Pingree*, 2008; *Lee and Brink*, 2010].

The presence of cold-core rings (CCRs) has been found more difficult to track by thermal imagery because their originally cold surface water is rapidly warmed by solar radiation. The enhanced surface stratification leads to a progressive warming of the surface and a CCR gradually becomes less distinguishable through surface temperature [*Kelly et al*., 2010; *Hausmann and Czaja*, 2012]. As cold water persists below the warm surface lid, CCRs can be detected by vertical profiles of temperature and salinity [*Dewar*, 1986]. In contrast, CCRs maintain its low SSS signature longer than the SST one [*The Ring Group*, 1981]. As such, satellite SSS imagery is expected to help longer term tracking CCRs.

Current remote sensing of SSS is being provided by the European Space Agency SMOS mission and by the NASA/CONAE Aquarius mission. These missions have been the first ones specifically designed to provide global, synoptic SSS observations by measuring the brightness temperature of the ocean surface at L-band (1.4 GHz). A quasi-global coverage is obtained every 3 and 7 days with an approximate spatial resolutions of 45 and 100 km for SMOS and Aquarius, respectively. One of the main differences between these two missions is that SMOS uses an interferometric radiometer to provide 1000 km wide, two-dimensional images of the ocean brightness temperature, in which each pixel is observed from a wide variety of incidence angles. In contrast, Aquarius consists of three L-band real aperture radiometers aligned with a 2.5 m real aperture antenna to sample the ocean surface along three fixed beams at three fixed incidence angles, i.e., 29.36°, 38.49°, and 46.29°.

As noticed by *Reul et al*. [2014], SMOS SSS maps can be used to identify rings of fresh anomalies south of the Gulf Stream. The superimposition of the geostrophic velocity fields derived from SSH maps on SMOS SSS maps (Figure 1b) confirms that the identified fresh anomalies indeed correspond to cyclonic eddies, suggesting that SMOS SSS maps are able to reveal the CCR SSS signature (lower values inside the eddy than in the surrounding waters). In contrast, the Aquarius L3-SSS map in Figure 1c reveals some small-scale features that, only in some cases, seem to be related with the CCRs observed in the SMOS image. As a summary, the comparison of Figures 1b and 1c reveal that the CCR SSS signature is clearly visible in the former (SMOS Level 3 map) while much less apparent in the latter (Aquarius Level 3 map).

In this study, a data fusion technique developed by *Umbert et al*. [2014], based on an image processing technique called singularity analysis [*Turiel et al*., 2008a], is used to improve the quality of Aquarius-based SSS maps and, in particular, to assess whether the salinity signature of CCRs can be well represented. For such purpose, three different templates are fused with Aquarius data, i.e., SMOS SSS, AVHRR SST, and AVISO SSH products. The resulting salinity maps will be thereafter called Level 4 (L4) products. The three different L4 maps will be validated both in terms of the difference with in situ data and in terms of CCR signature detection. The study region (Figure 1a) ranges from Blake Nose to Flemish Cap and mainly corresponds to the Gulf Stream region (80°W–40°W, 30°N–50°N), and the study period is the year 2012.

The structure of this paper is as follows: section 2 provides a brief description of the data. The data fusion and the vortex detection methodologies are presented in section 3. In section 4, the three different L4 products are compared against in situ data and assessed in their ability to resolve or reconstruct the salinity structure of CCRs. Finally, the summary and conclusions can be found in section 5.

2. Data Description

2.1. Sea Surface Salinity

Since the official Aquarius Level 3 (L3) products have a grid resolution of one degree, the detection and tracking of CCRs are difficult. Here we use Level 2 Aquarius SSS (version 3.0) data (http://oceandata.sci.gsfc.nasa.gov/Aquarius/) to produce L3 daily quarter-degree SSS maps with a temporal window of $\pm$3 days. Stringent filtering has been applied, keeping data only when SSS retrieval is known to be more accurate (wind speed lower than 15 m/s, low radio-frequency interference probability and low reflected galactic contamination). Due to the different spatial resolutions of the three beams, each beam is binned separately. All SSS data falling in the same grid cell of 0.25° $\times$ 0.25° are averaged with a weight inversely proportional to the squared Euclidean distance between the center of the beam and the center of the grid cell. Three different radii are used for each beam in accordance to their respective footprint sizes: 50, 70, and 90 km. The three resulting maps are averaged to produce a single composite map.

The SMOS product used here is that, discussed by *Reul et al*. [2014], the V02 daily composite, half-degree SSS maps obtained from the Ocean Salinity Expertise Center (CECOS) of the CNES-IFREMER Centre Aval de Traitement des Donnees SMOS (CATDS, http://www.catds.fr). Ascending and descending passes are bias-adjusted using a large-scale correction based on a 5° x 5° spatial filter derived from the monthly World Ocean Atlas 2001 climatology, temporally interpolated to the SMOS acquisition date [*Reul and CATDS-CECOS Team*, 2012]. To produce SMOS products with the same grid resolution as our L3 Aquarius SSS maps, we have generated SMOS L3-SSS maps by averaging 7 daily maps of the CATDS product and interpolating them onto a 0.25° grid using bilinear interpolation [*Press et al*., 1986].

Table 1. Description of the Data Used in the Study

Products	Input Data	Temporal Resolution	Grid Resolution (°)
Aquarius L3	Aquarius L2	1 day	0.25
SMOS L3	SMOS L2	1 day	0.25
AVISO ADT	Altimetry	1 day	0.25
AVHRR-OI	AVHRR	1 day	0.25
L4-SSH	Aquarius L3 + AVISO ADT	1 day	0.25
L4-SSS	Aquarius L3 + SMOS L3	1 day	0.25
L4-SST	Aquarius L3 + AVHRR-OI	1 day	0.25

Both SMOS and Aquarius can be used to detect the location of the haline front associated with the Gulf Stream between the shelf sea and the subtropical gyre (Figures 1b and 1c). Near the coast, salinity retrievals are less accurate due to signal contamination associated with the abrupt brightness temperature transition between the sea (~100 K) and the land (~220 K). This land-sea contamination effect is most noticeable in the SMOS data due to image reconstruction issues associated with the interferometric design of the instrument. In SMOS SSS maps, that contamination can extend up to several hundreds of kilometers offshore [*Zine et al*., 2007].

Another relevant aspect of the SMOS and Aquarius L-band measurements is the presence of radio-frequency interferences (RFI) which degrade the quality of the retrieved SSS maps. Although this frequency band (1.4 GHz) is allocated to the Earth Exploration Satellite Service, the first data acquisitions made by SMOS in the western North Atlantic Ocean evidenced high RFI occurrence. Due to military radar arrays installed over North America, SMOS data in the North Atlantic have been contaminated by RFI until the end of 2011. Since then, the switch-off of unauthorized emissions [*Daganzo-Eusebio et al*., 2013] (e.g., mostly radio devices that are emitting in the radio frequency band allocated for Earth observation purposes) within the protected L-band has led to a noticeable improvement of the data quality in this area. Despite the relatively large noise still present in the SMOS-derived SSS fields (salinity errors of about 0.3–0.4 in tropical and subtropical regions and 0.5 in cold regions, when compared against in situ salinity observations), their unprecedented spatial and temporal resolutions capability has already given interesting results such as the study of salinity variation in marginal seas [*Gierach et al*., 2013], ocean response to tropical cyclones [*Grodsky et al*., 2012; *Reul et al*., 2012] and the study of rain-induced surface salinity variability [*Boutin et al*., 2012].

2.2. Auxiliary Data

Delayed time merged Global Ocean Gridded Sea Level Anomalies (SLA) and the Absolute Dynamic Topography SSALTO/DUACS L4 products are used in this study (all relevant information about these products can be found at http://www.aviso.altimetry.fr/fileadmin/documents/data/duacs/Duacs2014.pdf). In short, optimal interpolation (OI) is used to generate combined daily quarter-degree maps that merge sea level observations from Cryosat-2, Jason-1, and Jason-2 satellites. In this paper, SLA maps are used for eddy-tracking, while the absolute dynamic topography maps are used as a template field for Aquarius SSS data fusion.

The SST data used in this work correspond to the Advanced Very High Resolution Radiometer (AVHRR) daily quarter-degree, optimally interpolated (OI) product of *Reynolds et al*. [2007], which is available at NOAA-NCDC (ftp://eclipse.ncdc.noaa.gov/pub/OI-daily-v2/). This product results from the application of OI to data from the 4 km AVHRR Pathfinder Version 5 time series (when available, otherwise operational NOAA AVHRR data are used) and in situ ship and buoy observations. The OI analysis is a daily average SST that is bias-adjusted using a spatially smoothed 7 day in situ SST average. Both day and night satellite fields are independently bias-adjusted.

To highlight the location of the CCRs, the daily 1/3° resolution surface current product from the Ocean Surface Current Realtime Analysis (OSCAR), described in *Bonjean and Lagerloef* [2002] and available at (http://www.oscar.noaa.gov), is also used. This global, surface (0–30 m) velocity field are estimated from TOPEX/Poseidon altimeter data, Special Sensor Microwave Imager (SSM/I) wind data, and the gridded SST product of *Reynolds et al*. [2007] merged by the means of a steady, quasi-linear model of the ocean mixed layer. In this work, the surface velocity fields are only used to highlight the position of the Gulf Stream rings and their rotation direction. All data products are summarized in Table 1.

2.3. In Situ Data

The in situ salinity data used were collected and made freely available by the Coriolis project and programs that contribute to it (http://www.coriolis.eu.org). We used four Thermosalinograph (TSG) data sets available during the period of the study by the following ships: Explorer (C6TN4), TARA (FVNM), Ronald H. Brown (WTEC), and the TMM Sinaloa (ZCDJ6). The TSG data are smooth with a running Hanning filter of half width of ~12.5 km (approximately half width of the quarter-degree grid resolution) to be properly compared with L3 and L4-SSS products. Due to the poor quality of SMOS and Aquarius SSS data near the coast (land-sea contamination), TSG data with distance from the coast smaller than 350 km were not considered.

2.4. Singularity Analysis

Singularity exponents of the maps are calculated using the same dedicated software presented in *Turiel et al*. [2008a]. The Barcelona Expert Center has issued a free web service that allows users to obtain the singularity exponents associated to any variable contained in a NetCDF file. The service can be reached through http://cp34-bec.cmima.csic.es/new-service-available-singularity-analysis/.

3. Methodology

3.1. Data Fusion

Remote sensing imagery of the ocean surface provides a synoptic view of the complex geometry of filaments and vortices advected by the turbulent flow. The repeated observation of such structures show that ocean circulation is dominated by mesoscale variability (space scales of 50–500 km, time scales of 10–100 days, and currents of a few kilometers per hour). The signatures of those filaments and vortices are present in various remotely sensed (scalar) variables as surface temperature, salinity, or chlorophyll. In *Isern-Fontanet et al*. [2007], it was discussed how the spatial structure of any tracer advected by the ocean flow inherits some properties of the underlying flow dynamics. This is due to the interaction between coherent vortices that, in a turbulent flow, continuously stretch and fold small-scale filaments ejected from vortex cores, generating small-scale gradients between eddies. This leads to a geometrical arrangement of the flow as a hierarchy of fractal sets, called singularity manifolds, each one of them associated to a singularity exponent [*Turiel and Pérez-Vicente*, 2005; *Turiel et al*., 2008a]. In general, the singularity exponents reveal geophysical patterns as well as image artifacts that are not directly visible from the original satellite images.

A key element in the application of the multifractal formalism [*Frisch*, 1995] is the ability to decompose the signal into different patterns or fractal components, each one being characterized by a value of the singularity exponents $h(\vec{x})$. The components can be classified from the most singular, associated with the sharpest transitions, to the least singular, associated with smooth transitions [*Turiel and Parga*, 2000]. Given a scalar s, its singularity exponents can be derived from the wavelet projections of the gradient of the signal. Given a wavelet ψ, we define the wavelet projection of s at a given point $\vec{x}$ and for a given scale r, denoted by $T_\psi|\nabla s|(\vec{x},r)$, as:

$$T_\psi|\nabla s|(\vec{x},r)=\int d\vec{y}\,|\nabla s|(\vec{y})\,\frac{1}{r^2}\,\psi\left(\frac{\vec{x}-\vec{y}}{r}\right).$$

The wavelet projection is the convolution of the wavelet with the gradient of the signal s. The dispersion of the wavelet can be increased or reduced by increasing or reducing the variable r. Hence, a wavelet projection averages the gradient content around the point x at a distance modulated by r. The signal s has a singularity exponent $h(\vec{x})$ at a given point $\vec{x}$ if the following relation holds:

$$T_\psi|\nabla s|(\vec{x},r)=\alpha(\vec{x})r^{h(\vec{x})}+o\left(r^{h(\vec{x})}\right), \tag{1}$$

where the term $o\left(r^{h(\vec{x})}\right)$ means a term that is negligible in comparison with $r^{h(\vec{x})}$ when the scale r goes to zero. The singularity exponent $h(\vec{x})$ at the point $\vec{x}$ can be computed by performing a log-log regression between $\ln\,(T_\psi|\nabla s|(\vec{x},r))$ and $\ln\,(r)$ from r_0 up to an appropriate scale. Application of this method to ocean variables [*Turiel et al*., 2005; *Isern-Fontanet et al*., 2007; *Turiel et al*., 2008b] has shown that ocean variables exhibit a multifractal structure and scalar variables such as SST and chlorophyll concentration have the same singularity exponents [*Lovejoy et al*., 2001; *Nieves et al*., 2007].

The temporal evolution of SSH is different from that of SST or SSS indicating that evolution of SSH to first order cannot be explained by horizontal advection alone. For instance, the SSH response to changes in large-scale winds can be described as long first baroclinic mode Rossby waves whose evolution depends on the meridional advection of the background potential vorticity gradient. This term is important at large spatial scales. However, horizontal advection is the dominant process contributing to the creation of localized strong gradients in the mesoscale SSH field. Now when advection is the only term inducing sharp transitions on a given passive or nonpassive scalar, singularity exponents will be related to streamlines [*Isern-Fontanet et al*., 2007; *Turiel et al*., 2009], independent of the particular scalar of choice. The regions of largest gradients in the SSH are associated with mesoscale fields where the Rossby number is large (we define the Rossby number as U/fL where U is the velocity scale, L is the length scale, and f is the Coriolis parameter). As advection becomes important at large Rossby numbers, we expect that the singularity fields of SSH will be similar to those of other scalar fields.

The fusion algorithm introduced by *Umbert et al*. [2014] assumed that the singularity lines of the ocean variables coincide. The results showed that, to a good extent, the singularities of SST and SSS are very similar. As a consequence of the correspondence between the singularity exponents of two scalars, a functional relation between the module of the gradients of both scalars must exist. *Umbert et al*. [2014] devised a data fusion algorithm by assuming that the local function relating the gradients can be approximated by a local linear relation between the two variables. This approach allows exploiting a high-quality variable field, called the template and noted as t, to improve the spatial coverage and the signal-to-noise ratio of a variable s. The new, fused variable $\hat{s}$ is constructed by applying:

$$\hat{s}(\vec{x})=\hat{a}(\vec{x})t(\vec{x})+\hat{b}(\vec{x}), \tag{2}$$

where $\hat{a}(\vec{x})$ and $\hat{b}(\vec{x})$ are the estimators of the functions that define the local linear relation. These estimates are obtained from the values of s and t by performing linear regressions weighted around each point as in *Nieves et al*. [2007]. Due to the assumption of local linearity and the process of calculating the estimators a and b, the maps resulting from the application of the fusion algorithm are more smooth when compared to the original fields [*Turiel et al*., 2014].

3.2. Vortex Identification

The daily SLA maps provided by AVISO are used to locate cyclonic (and anticyclonic) eddies using a SSH-based mesoscale eddy tracking software, called *py-eddy-tracker*, which is described in *Mason et al*. [2014]. The *py-eddy-tracker* program works with a smoothed version of the high-pass filtered SLA. The high-pass filter is a Gaussian filter with a zonal radius of 10° and a meridional radius of 5°. Contours of SLA are computed for levels ranging from −100 to 100 cm at every 0.25 cm intervals. For a given SLA level, eddies are identified as closed contours which verify a set of geometric criteria (further details on the algorithm can be found in *Mason et al*. [2014]). As input, the code requires sequential maps of SLA. Output files contain eddy properties, including position, radius, amplitude, and azimuthal (geostrophic) speed. Additionally, a tracking record of each eddy through time is produced.

4. Results and Discussion

The data fusion algorithm is applied to daily Aquarius L3-SSS maps for the year 2012 using three different templates, SSH, SSS, and SST, described in section 2. The resulting L4-SSS maps will be called hereafter L4-SSH, L4-SSS, and L4-SST, respectively.

Figure 2 shows an example of a L3-SSS map from Aquarius and the three corresponding Level 4 maps from 23 August. The data fusion algorithm reduces the frontal salinity gradients and smooths the Aquarius L3 map (reduces the level of noise due to the relatively poor Aquarius sampling). The OSCAR velocity vectors are superimposed to indicate the position of the cyclonic rings south of the Gulf Stream. The average radius of the cyclonic eddies automatically detected by *py-eddy-tracker* is about 135 km, with half of the eddies having a radius between 106 km and 155 km (the minimum radius is 80 km and the maximum 285 km). We assume that cyclonic eddies south of the GS of that size can only be formed from detached meanders of the GS as CCRs. The expected SSS signature in the rings core can indeed remain quite similar to the initial conditions for 1–3 months after the rings formation [*The Ring Group*, 1981]. Thus, a fresh anomaly in the center of the CCRs (w.r.t. outside of the rings) is expected.

In Figure 2a, the Aquarius L3 map shows no clear SSS signature related to the cyclonic rings (as delineated by the OSCAR velocity field), while the Level 4 maps do exhibit the expected fresh anomaly signature.

10.1002/2014JC010466

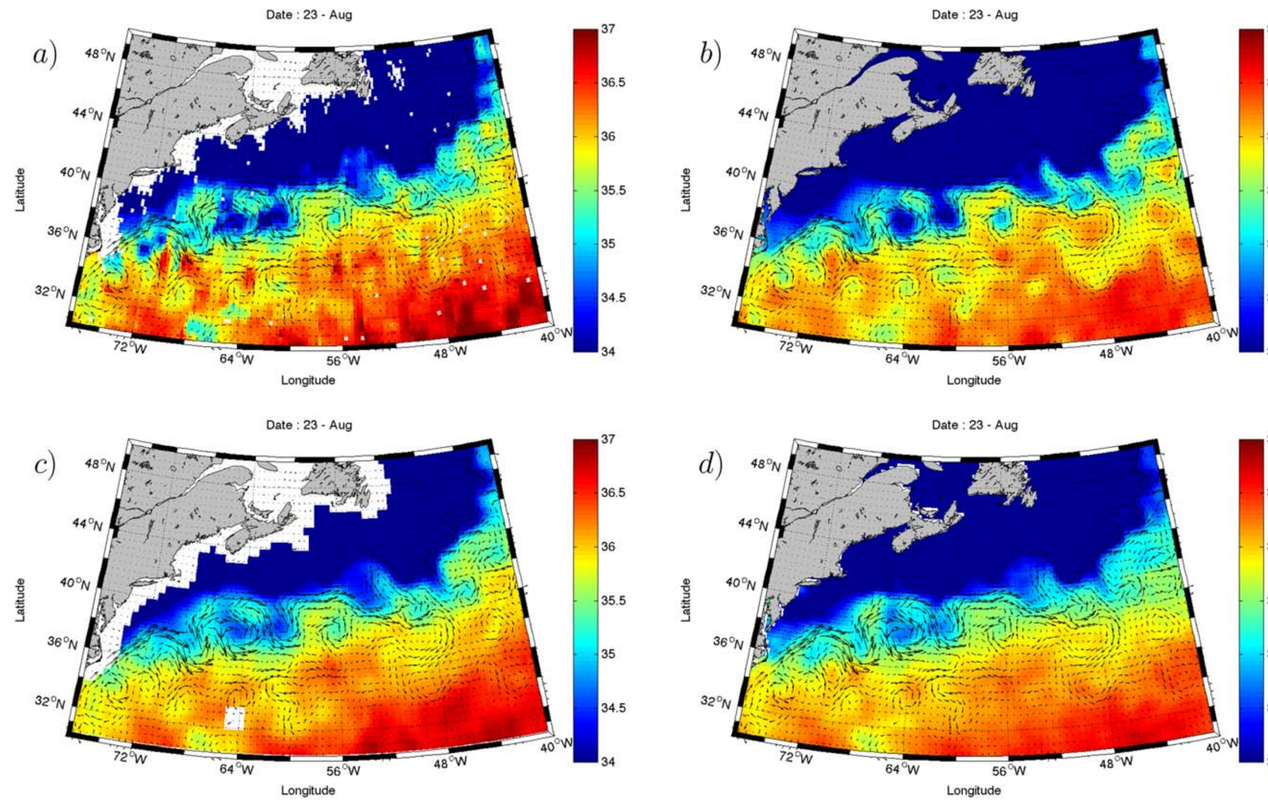

Figure 2. Sea surface salinity for the 23 August with OSCAR velocities. Aquarius L3-SSS field (a) compares with Aquarius L4-SSS using the three different templates: (b) AVISO SSH, (c) SMOS SSS, and (d) AVHRR SST.

However, not all L4 products show the same amount of fresh anomalies associated with CCRs. In particular, the L4-SSH (Figure 2b) shows a larger amount of fresh anomalies as compared with the L4-SSS (Figure 2c). Indeed, the L4-SSH product exhibits a salinity signature, which coincides with most of the Gulf Stream meanders and CCRs depicted by OSCAR velocities (Figure 2b). Finally, the L4-SST product does not reproduce a clear fresh anomaly for most of cyclonic rings (Figure 2d). The main drawback of using SST as a template in this region is linked to the fact that remotely sensed SST does not delineate the cold rings of the Gulf Stream as the SST response in the shallow mixed layer results in heat fluxes veiling these mesoscale signals. This is especially true in summer.

A validation of the resulting SSS products is performed using in situ TSG salinity data from four different cruise campaigns carried out during 2012. Figure 3a shows the difference between the L4-SSH and the TSG observations. The histograms of the differences between the TSG SSS data and the different satellite products are shown in Figures 3b–3f. The Aquarius L3 (Figure 3b) and the SMOS L3 (Figure 3c) present the largest discrepancies from the in situ observations, both in terms of the standard deviation and the interquartile range (iqr). In contrast, all L4 data fusion products (Figures 3d–3f) present a reduction of both the central value of the difference (mean or median) and the error when compared with the L3 products (Figures 3b and 3c). Of all the fused products, the L4-SSH (Figure 3d) is the closest to the in situ data (median of 0.001 and iqr of 2.26), while the L4-SSS (Figure 3e) presents the worst scores (median on 0.096 and iqr of 0.32), quite close to those of the Aquarius L3 product (Figure 3b).

Figure 4 shows a TSG transect from the Explorer vessel in the period 13–17 August. In Figure 4a, the transect (thick solid line) is drawn on top of the L4-SSH map from 15 August. The SSS map suggests that the Explorer TSG transect crosses the GS as well as two structures with apparent CCR signature (those around 56°W and around 50°W). Note that west of the GS (65°W, 40°N), the in situ SSS is higher than 35.5 indicating the presence of an WCR. The various salinity products show this salty anomaly and the location of the saline front associated with the GS (61–62°W, 40°N).

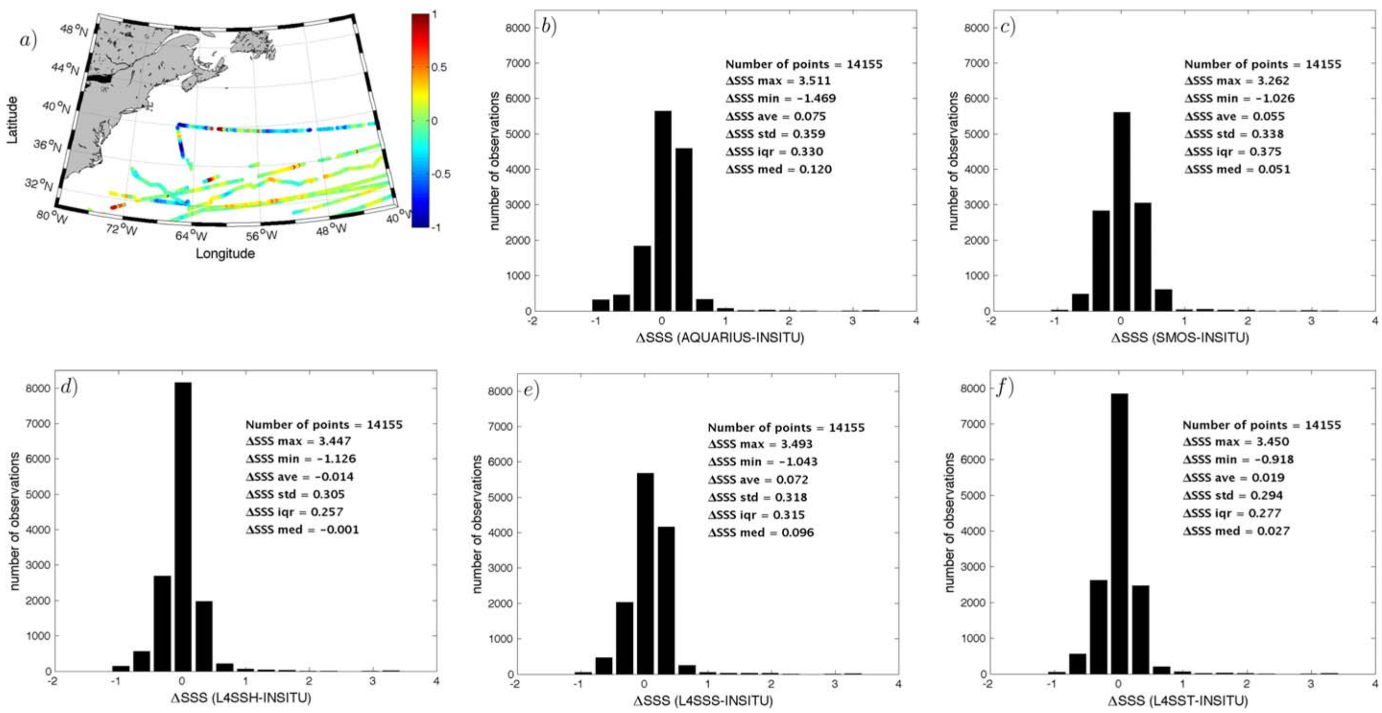

Figure 3. (a) L4-SSH product minus TSG in situ salinity. SSS difference histogram with in situ data with (b) Aquarius L3-SSS, (c) SMOS L3-SSS, (d) L4-SSH, (e) L4-SSS, and (f) L4-SST.

In Figure 4b, the SSS data along the transect are shown for all the salinity products. The local salinity minimum around 56°W, as indicated by the TSG data, is barely noticeable in the Aquarius L3 product, and completely missing in the SMOS L3 and the L4-SSS products. The L4-SST product displays a slightly shifted (at 55°W) and secondary minimum, while the L4-SSH displays a well-defined salinity minimum at the location of the CCR, i.e., in line with the TSG data. Although the amplitude of the minimum salinity is weaker than that observed by in situ data (almost 1.5), the salinity difference between the inner-core and its western limit is as large as 1. On the other hand, the TSG salinity minimum located at 50°W is completely missing in the Aquarius L3 field and the L4-SST. Both SMOS L3 and the L4-SSS detect, a negative salinity anomaly, although slightly displaced toward the west. Again, the L4-SSH product recovers the low salinity anomaly, showing a salinity difference between the CCR outer and inner parts larger than 0.5. While this difference is again smaller than that of the in situ data ($\sim$1), it is the largest among the different SSS products considered here.

The normalized variability of the three templates (AVISO SSH, SMOS SSS, and AVHRR SST) in the same transect is shown in Figure 4c. AVISO SSH help to achieve both a better position and amplitude of the CCRs. Compared with Figure 4b, it is clear that the fused product inherits the spatial modulation of the template used.

Due to scarcity of the in situ data, the presence, size, and center of the eddies are obtained from sea level anomalies by using the *py-eddy-tracker* algorithm (section 3.2). This will be used to study the spatial and temporal coherence of the retrieved SSS field patterns/structures in all the locations where cyclonic eddies are identified from altimetry. Again, it is assumed that all cyclonic eddies south of the GS are CCRs, shed from GS instabilities. Figure 5a shows the SSH corresponding to 1 June 2012. The black dots correspond to the center of the eddy identified by *py-eddy-tracker* for such a date. The map also shows the initial eddy location (open black circle) and the path followed by each eddy (black line). The effective radius of each of the eddies identified by the *py-eddy-tracker* is shown with black crosses in Figure 5b. In 2012, there were a total of 7949 cyclonic eddies in the daily SLA snapshots in the region (which actually correspond to 454 different eddies automatically detected and tracked). Note that not all cyclonic structures detected by *py-eddy-tracker* correspond to a closed structure in SSH; sometimes they correspond to Gulf Stream meanders.

The expected SSS structure of CCRs has a negative salinity gradient between the center and its surroundings, as the ring contains fresh water from the north of the Gulf Stream. Figure 6a displays a section of SSH and Aquarius L3-SSS fields across the vortex called R1 (Figure 5a). The vertical lines indicate the position of

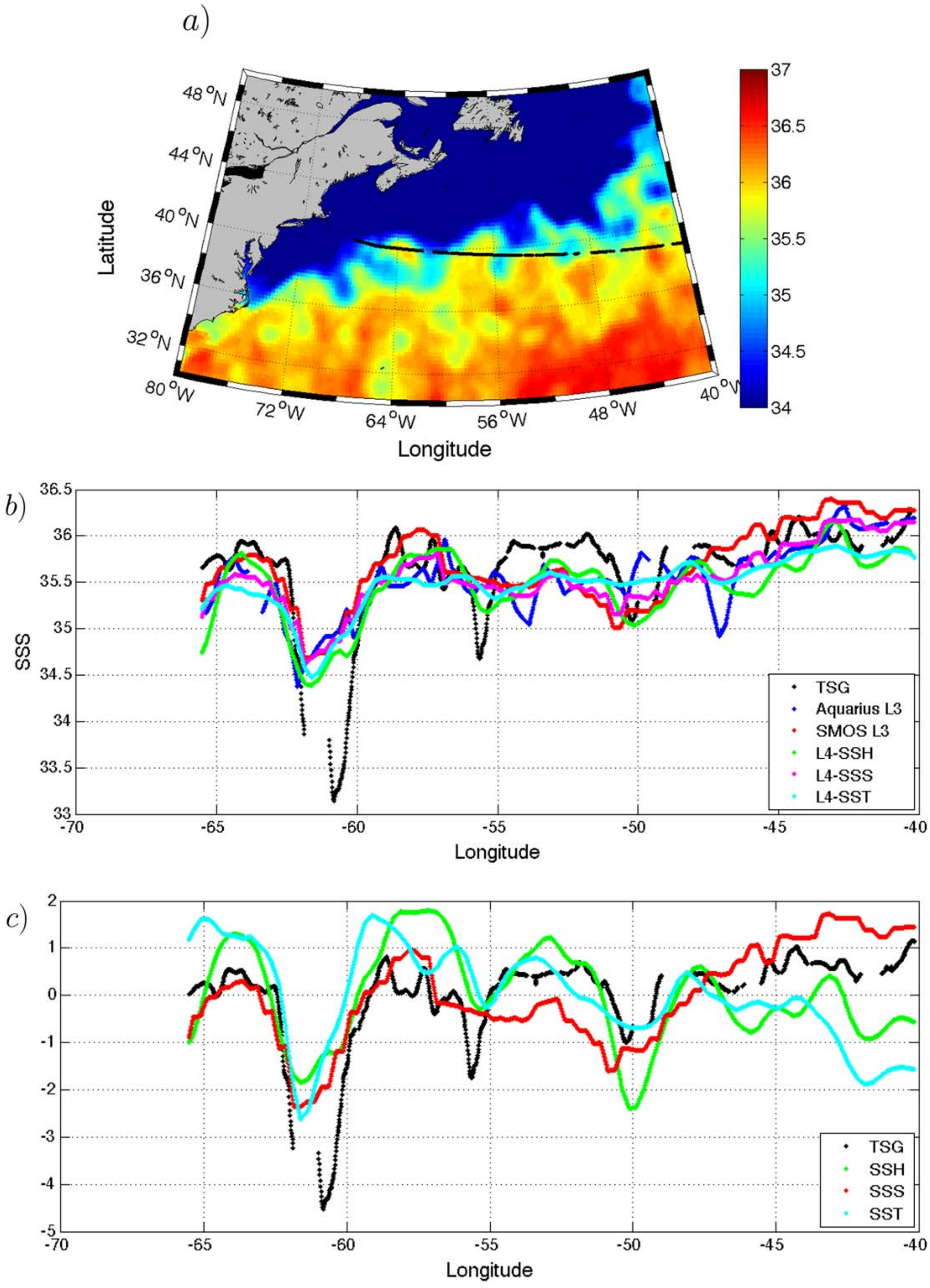

Figure 4. (a) L4-SSH for the 15 August with TSG positions of Explorer from 13 to 17 August 2012 in black dots. (b) Comparison of in situ data along the transect in Figure 4a with Aquarius L3-SSS and L4-SSS maps of 15 August. (c) Comparison of AVISO SSH, SMOS SSS, and AVHRR SST templates along the same track, centered, and normalized by their variability along the track.

the center and the radius of the eddy found by the *py-eddy-tracker*. The graph reveals only a small correspondence between the Aquarius L3 salinity field and the SSH minimum across the R1 ring. Although less noisy than the Aquarius L3, the L4-SSS product (Figure 6e) also shows a small correspondence with the SSH product. In contrast, the salinity transects of L4-SSH (Figure 6c) and L4-SST (Figure 6g) reveal a salinity minimum well aligned with the SSH minimum.

 10.1002/2014JC010466

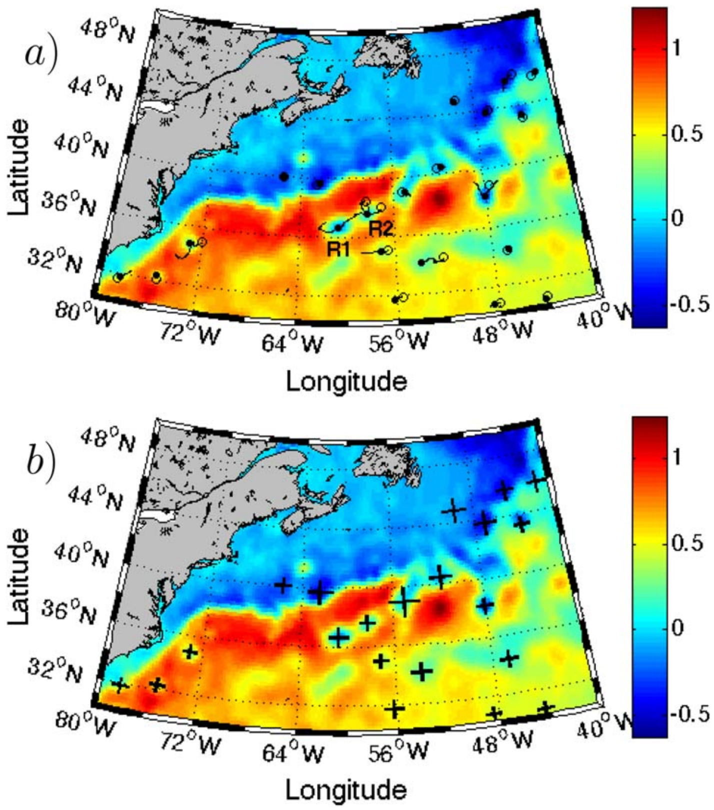

Figure 5. (a) AVISO SSH (m) background with black dots representing eddy centers found by *py-eddy-tracker* for 1 June, the initial eddy location (open black circle) and the path followed by each eddy (black line). (b) SSH field for the same day with the position and amplitude of the detected eddies with the size of the crosses indicating the size of the SSH anomaly associated with the eddy.

The salinity gradient along all detected cyclonic eddies (the difference between the center and the outer part of the ring) is calculated for the four salinity products (Aquarius L3 and the three Level 4 products). The salinity outside the ring is estimated by considering the median of the four grid points located at the radius distance from the eddy center (note that eddies have different radius values and these can also vary with time). The salinity gradient has an average value of −0.09 for Aquarius L3 (Figure 6b), −0.35 for L4-SSH (Figure 6d), −0.07 for L4-SSS (Figure 6f), and −0.14 for L4-SST (Figure 6h). The L4-SSH gradient amplitude estimates are in average 2.5–5 times the value estimated from the other products. No noticeable improvement in resolving cyclonic-eddies fresh anomaly structures is achieved by using the SMOS L3-SSS as template (i.e., L4-SSS).

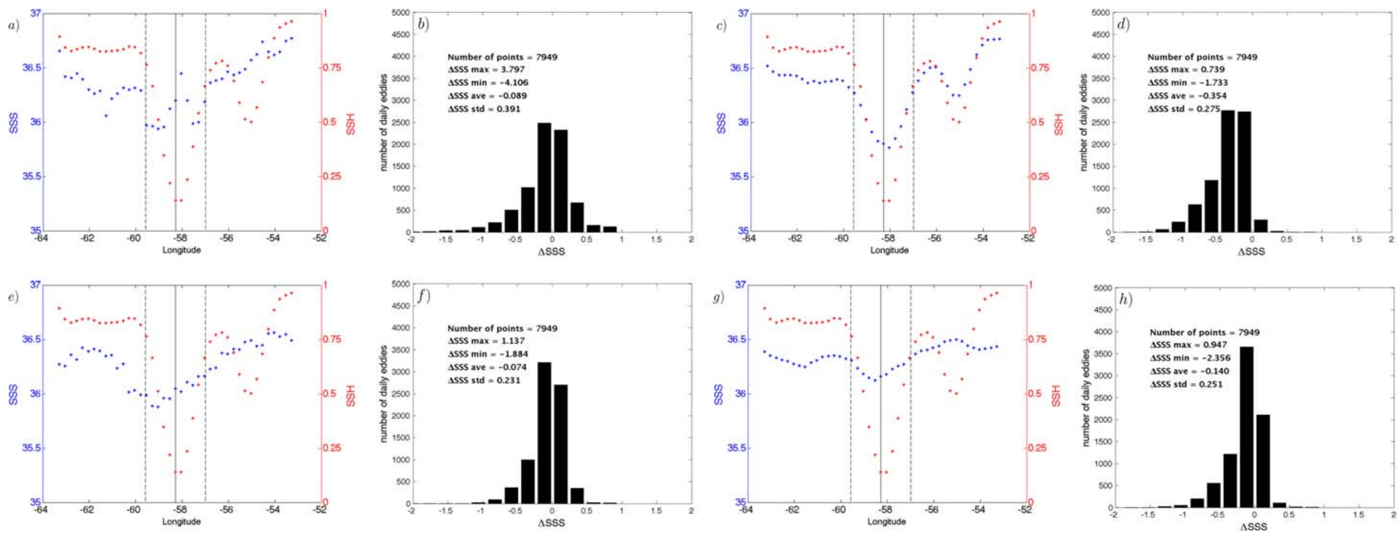

Figure 6. Section along the vortex R1 (a) shown in Figure 5a for sea surface height (m) and sea surface salinity ((a) Aquarius L3, (c) L4-SSH, (e) L4-SSS, and (g) L4-SST) 1 June 2012. Vertical lines indicate the center (solid black line) and the ±1 radius of the eddy (dashed lines). SSS difference histogram between inside and outside the cyclonic vortex found in the 365 days of the analysis for (b) Aquarius L3, (d) L4-SSH, (f) L4-SSS, and (h) L4-SST.

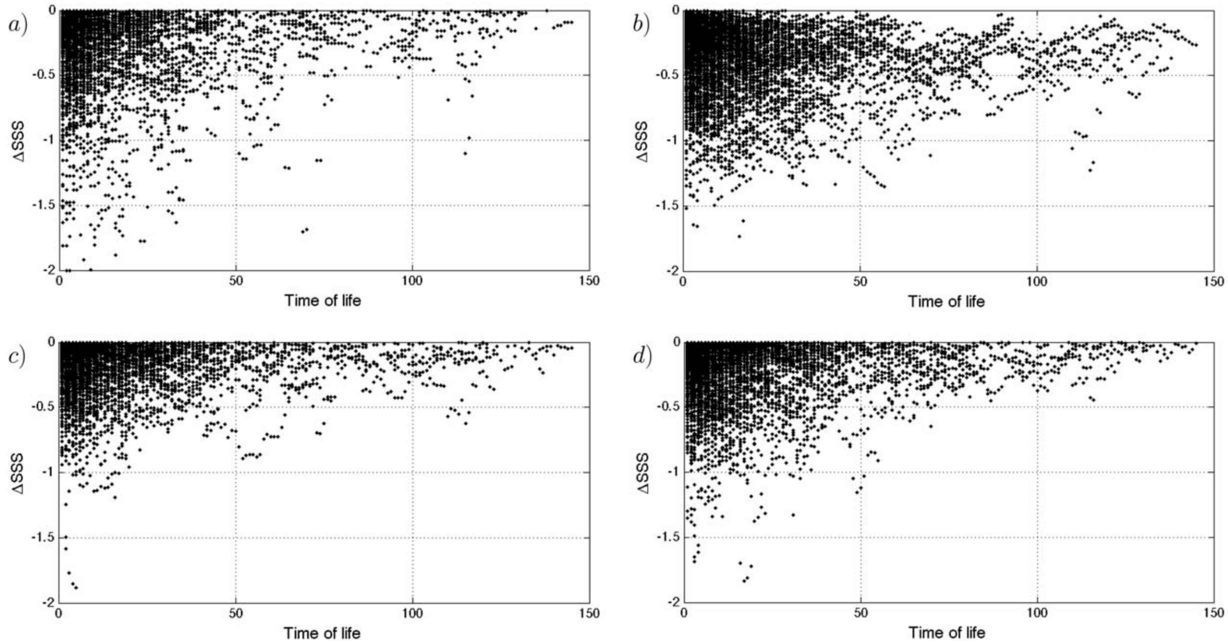

Figure 7. Temporal evolution (days) of SSS gradient in CCRs detected by (a) Aquarius L3, (b) L4-SSH, (c) L4-SSS, and (d) L4-SST over the entire study domain.

The total number of cyclonic eddies detected in SLA daily images by *py-eddy-tracker* is 7949. In SMOS and Aquarius L3 maps, only 4642 and 4413 eddies (58% and 56% of the total) have an associated fresh core, respectively. In the Level 4 products, the number of fresh cores are 7621 (96%), 5632 (71%), but only 4616 (58%) for L4-SSH, L4-SST, and L4-SSS, respectively. Figure 7 shows the scatter plots of the salinity gradients along these fresh-core cyclonic structures for the Aquarius L3 (Figure 7a) and the different Level 4 products (Figures 7b–7d). The salinity gradient is plotted as a function of the age of the dynamic cores provided by *py-eddy-tracker*. Note that most of the SSS products accumulate values close to zero gradient (i.e., very close salinity values inside and outside the cyclonic gyre) at any age. The exception is for the L4-SSH product, which only has near zero gradient values for young eddies (less than 20 days old), but not for long lasting eddies. The four SSS products contain a significant amount of fresh-core cyclones with initial salinity anomalies larger than 1. As expected [*The Ring Group*, 1981], the salinity anomaly decreases with the age of the eddy, becoming lower than -0.5 for almost all eddies older than 2 months. Interestingly, the long lasting eddies (older than 2 months) in the L4-SSH product show a persistent or slowly decreasing negative anomaly of about -0.3 in average, remarkably larger than that of the other products. The reason lies in the bigger amplitude variation of SSH between the inside and outside of the CCR compared to the other templates as illustrated in Figure 4c.

Time series of SSS inside and outside specific rings (vortex R1 and R2 (Figure 5a)) are shown in Figure 8 for Aquarius L3 (black), L4-SSH (red), L4-SSS (blue), and L4-SST (green). By looking at the temporal evolution of CCR R1 (Figure 8a), first detected on 6 March at lat = 38.42°N and lon = 58.31°W, the L4-SSH product is characterized by a (negative) 0.4–0.8 salinity difference between the core and outer parts of the CCR. According to the L4-SST product, the center of the CCR is fresher than its surroundings by about 0.1–0.3 salinity difference until day 38, when the salinity difference changes sign, while in L4-SSH product, the salinity inside the CCR is systematically lower than that outside the CCR over the full period of 46 days. Therefore, L4-SSH provides a geophysically consistent SSS structure in line with the cyclonic ring circulation. When looking at the temporal evolution of SSS according to the Aquarius L3 and the L4-SSS products, the difference between the SSS inside and outside the CCR is not systematically negative, and changes sign several times over life time period of 46 days. This is an indication that the CCR structure is not well reconstructed by the mentioned products, since conditions in the core of the ring should be quite similar to Slope Water (north of the GS) conditions for 1–3 months before mixing and heating modify surface waters [*The Ring Group*, 1981].

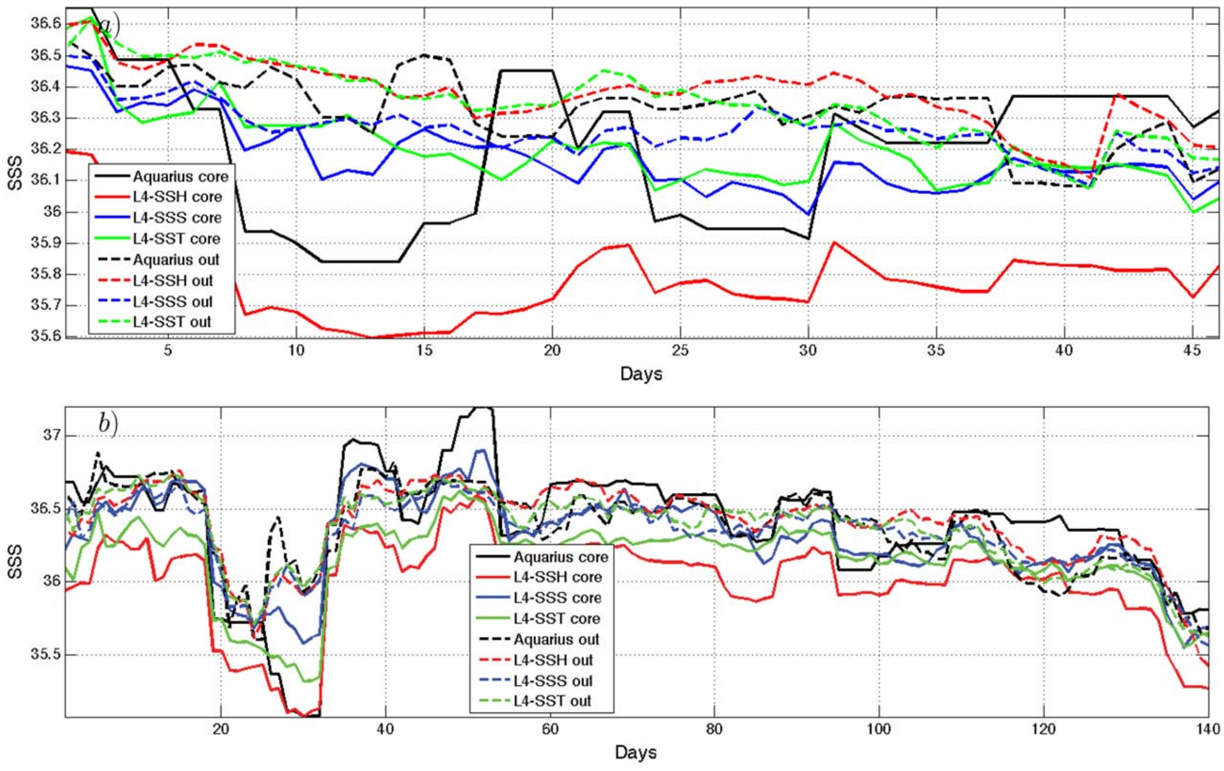

Figure 8. Temporal evolution of SSS inside (solid lines labeled "core") and outside (dashed lines labeled "out") the CCR for Aquarius L3 (black), L4-SSH (red), L4-SSS (blue), and L4-SST (green). (a) CCR starting on 6 March (R1 in Figure 5a). (b) CCR starting on 12 May (R2 in Figure 5a).

Similar results are obtained when looking at the temporal evolution of CCR R2 (Figure 8b), first detected on 12 May at lat = 37,96°N and lon = 57,06°W. The temporal persistence of negative salinity anomalies patterns, consistent with the cyclonic rings found by *py-eddy-tracker*, is much larger for L4-SSH data (the entire time period of 140 days found by *py-eddy-tracker*) than for Aquarius L3 (0 days), L4-SSS (2 days), and L4-SST data (115 days). Similar results are obtained when other rings are studied. We hence conclude that the L4-SSH product best represent the CCRs SSS signature.

Maps of the singularity exponents (calculated as in *Turiel et al*. [2008a]) are generated from Aquarius L3, AVISO SSH, SMOS L3, AVHRR SST, L4-SSH, L4-SSS, and L4-SST maps in Figure 9. The data correspond to 1 June 2012. As discussed in section 3.1, the singularity exponents provide information about the flow and thus should be independent of the particular scalar from which they are derived, i.e., they are basically related to a component of the signal which is common to all ocean scalars (the advection term). In practice, due to errors, noise, and limitations of the algorithm used to estimate the singularity exponents, some of the singularity exponents associated with the streamlines of the flow are lost [*Turiel et al*., 2009]. Previous studies show that the singularity fronts (bright white lines) of high-quality ocean surface remote sensing maps are very much aligned with altimeter-derived surface currents. The singularity maps shown in *Turiel et al*. [2009] are very similar to those in Figure 9b, indicating that AVISO SSH is indeed a geophysically consistent product. On the contrary, it is clear that the Aquarius L3 product (Figure 9a) is noisier and unstructured, i.e., note that the large amount of quasi-meridional singularity front lines, which correspond to the different ascending and descending satellite passes (in other words, those lines are image artifacts created by poor sampling). Furthermore, not even the main large-scale geophysical structures (such as the Gulf Stream) are well resolved in Figure 9a. The singularity map of SMOS L3 (Figure 9c) appears less noisy in comparison with the Aquarius L3; however, only the large-scale structures can be recognized and many sampling artifacts (quasi-meridional singularity lines) are also present.

The singularity map of the L4-SSH product (Figure 9e) shows that the fusion algorithm is able to restore much of the singularity structure present in the SSH map. On the other hand, as expected, the L4-SSS

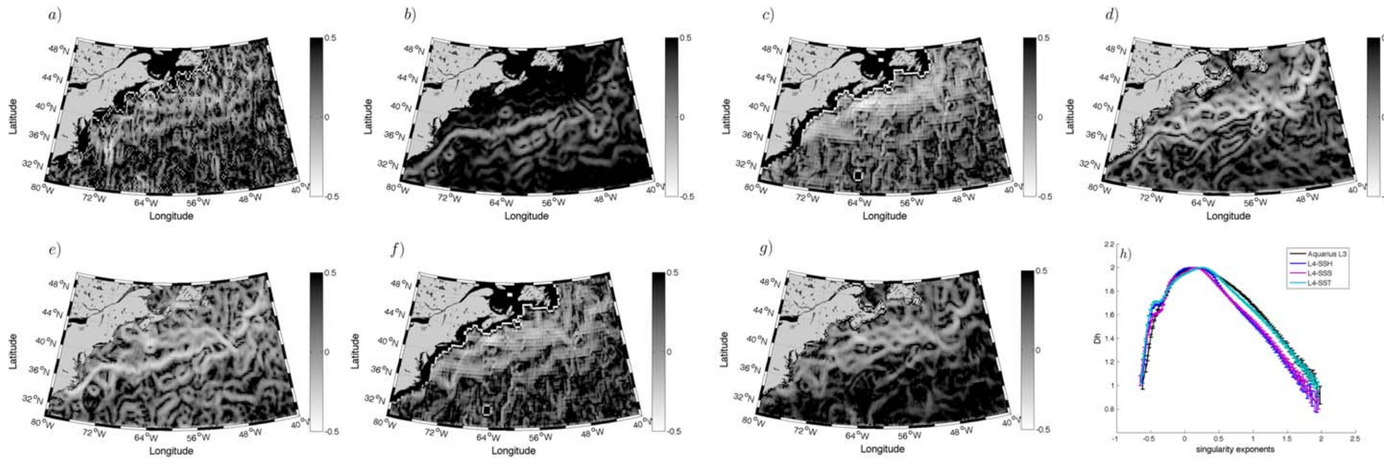

Figure 9. Singularity analysis exponents maps of (a) Aquarius L3, (b) AVISO SSH, (c) SMOS SSS, (d) AVHRR SST, (e) L4-SSH, (f) L4-SSS, and (g) L4-SST. (h) Singularity spectra for Aquarius L3 and L4 products corresponding to the 366 days under study.

singularity map (Figure 9f) shows most of the artifacts present in the SMOS SSS singularity map (Figure 9c). As such, the L4-SSH product is clearly more geophysically consistent than the L4-SSS product. The L4-SST map (Figure 9g) represents an intermediate situation, for which singularity exponents are better defined than in the L4-SSS map but are not as rich as in the L4-SSH map.

To fully characterize the statistical behavior of changes of scale in multifractal systems, the singularity spectrum [*Parisi and Frisch*, 1985; *Frisch*, 1995; *Turiel and Parga*, 2000] is used. The singularity spectrum of a multifractal system, $D(h)$, is a scale-invariant function that represents the distribution of the singularity exponents [*Turiel and Parga*, 2000]. Its shape is linked to the cascade dissipation [*Turiel et al*., 2008a] and it should be the same for all parameters advected by the same flow. The computation of the singularity spectra is done as in *Turiel et al*. [2006]: the empirical histogram of the values of singularity exponents h is log-transformed and normalized to compute $D(h)$. The singularity spectra associated with the products used in this paper can be found in Figure 9h. The method also allows evaluating the error bars associated with sampling size (note that error bars are shown in the Figure 9h). These error bars do not account though for the uncertainty associated with the method itself, which is estimated to be about 0.1 [*Turiel et al*., 2006, 2008a].

The right part of the spectrum (positive singularity exponents) corresponds to the less singular values, which are represented as dark areas in the maps of Figure 9. Large differences exist among the SSS products in this part of the spectrum because the less singular (i.e., positive) values are associated with the more regular and smooth parts of the function, and are therefore more sensitive to noise and artifacts. The left part of the spectrum corresponds to the most singular (negative) values, corresponding to the brightest (whitest) areas in the singularity exponents maps of Figures 9a–9g. The spectra of L4-SSH and L4-SSS are very close on the right-hand side of the spectrum, but the difference with all the other is larger than the error bar associated with both the sampling size and the uncertainty in the method used to calculated singularity exponents. This is probably an indication that the other products (Aquarius L3 and L4-SST) do not represent well the distribution of more regular values. Singularity spectra derived from Aquarius L3 and L4-SST are relatively wide (the spectra width can be measured as the distance between the two intercepts of the horizontal line $D = 1$), as compared to the universal class of singularity spectrum presented in *Pont et al*. [2009]. Negative values identify regions of abrupt changes in the flow, such as fronts or filaments, but also, as mentioned earlier, potential sampling artifacts. In this part of the spectrum, all the products are closer to each other, except for an excess bump just above -0.5 which is typical of sharp edges, e.g., coastlines and, in some products, artifacts like orbital gaps.

5. Conclusions

The ability of Level 4 SSS maps derived from Aquarius L3 data to recover mesoscale processes has been investigated. The region under study is the Gulf Stream western boundary current, where mesoscale activity in form of meanders, filaments, and eddies has been well documented. The ESA SMOS L3 maps can be used for such purpose since, despite some processing artifacts, they do indeed reveal the SSS signature of such mesoscale phenomena [*Reul et al*., 2014]. In this study, we have focused on the ability of different L3 and L4 remotely sensed SSS products to reproduce cyclonic rings detached southward from the mean flow of the Gulf Stream current, known for having a cold, fresh water core as a result of the exchange between water masses separated from this frontal area.

It has been shown that Aquarius L3 data poorly resolve the cold-core rings and their evolution due to the relatively poor spatial and temporal resolutions. To improve the SSS signature estimation of such mesoscale features, a fusion algorithm based on the multifractal properties of ocean scalars has been applied to Aquarius data. The method merges the information coming from two different ocean scalars to generate a new product of improved quality and resolution. One of the two scalars, denoted as *template*, is assumed to be of higher quality than the other one, denoted as *signal*. The template is used to improve the quality of the signal by restoring the singular structure that both scalars should share. Several templates, i.e., AVISO SSH, SMOS SSS, and AVHRR SST, are used for comparison purposes.

A first quantitative validation of the different fused products using in situ SSS data as reference has shown a reduction in systematic (bias) and random errors in the L4 fused SSS products in comparison with the Aquarius and SMOS L3 products. Also, the expected relatively fresh anomaly inside (w.r.t. outside) the CCRs observed by in situ data is better reconstructed by the L4 fused SSS products.

To assess the ability of the fused products to recover the CCRs salinity structure, an eddy detection method has been used. This method allows the detection of cyclonic vortices detached from the Gulf Stream main trajectory using SLA maps. A mean decrease in salinity between the ring center and the outside (i.e., negative anomaly) of about 0.3–0.4 is found for the different products in the year 2012. The Aquarius L3 product fused with SSH data (L4-SSH) is clearly superior to the rest of the products, i.e., Aquarius L3, SMOS L3, Aquarius fused with SMOS SSS (L4-SSS), and Aquarius fused with SST (L4-SST) in resolving the CCRs salinity signature and in monitoring the CCRs evolution, by showing both larger negative SSS anomalies and larger temporal persistence of such anomalies. Moreover, the L4-SSH CCR negative anomalies are significantly better aligned with those observed by several in situ cruise campaigns than those from the other L3 and L4 products.

The singular analysis of the different SSS maps has been carried out to validate the fusion method applied to Aquarius SSS data. The fusion method is indeed correctly padding the singularity structure of the template on the fused images. Thus, Aquarius SSS benefits from the geophysical consistency of the SSH data. In contrast, using a noisier template with sampling artifacts like SMOS L3-SSS results in a less geophysically consistent product.

Although the L4-SSH product clearly shows the best results in terms of CCR persistence and validation against TSG data, poor altimetric sampling can lead to spurious cyclonic eddies and therefore spurious CCRs/negative SSS anomalies in the L4-SSH product. A more in-depth analysis is recommended to quantify missing alarm and false alarm rates.

This study has focused on how well the different data fusion products recover the CCR SSS signature. As mentioned in section 1, satellite detection of warm-core rings is already well documented but presents certain limitations, e.g., poor sampling (since high-resolution SST imagery is affected by the presence of clouds). A similar study to that presented here could be carried out with WCRs. Several issues may however arise, such as land-sea contamination (when rings are within a few hundred kilometers from the coast) or the low quality of SSS products in cold waters, which may negatively impact the quality of the fused products. However, a dedicated study is recommended to assess the ability of the proposed data fusion algorithm to observe the WCRs SSS signature and check whether it provides any added value to the current satellite products.

The GS is one of the most studied oceanic currents in the world. Its influence on ocean circulation and climate has been well established, but additional efforts are still needed to better monitor and understand its variability. This study has illustrated a regional application of a singularity analysis-based fusion technique to improve CCR tracking from Aquarius SSS data. The application of this algorithm at global scale and daily basis can provide new insights on the role of sea surface salinity in the Earth's water cycle and ocean dynamics.

Acknowledgments
This work has been funded by the Spanish Ministry of Economy through the National R+D Plan by means of MIDAS-7 project AYA2012–39356-C05-03. M. Umbert is funded by the Spanish Ministry of Economy through FPI grant BES-2011–047173. L. Thompson was supported by NASA through grant NNX08AR30G (Ocean Surface Topography Science Team) with the University of Washington. We gratefully acknowledge the insightful and helpful reviews, comments, and suggestions by three anonymous reviewers that helped improve the content and readability of the paper. The authors acknowledge AVISO service website maintained by CLS for making publicly available their sea surface height data. Daily composite, half degree SMOS SSS data were obtained from the Ocean Salinity Expertise Center (CECOS) of the CNES-IFREMER Centre Aval de Traitement des Donnees SMOS (CATDS). Level 2 Aquarius SSS (version 3.0) data were obtained at http://oceandata.sci.gsfc.nasa.gov/Aquarius/. Ocean Surface Current Realtime Analysis product was obtained at http://www.oscar.noaa.gov. Advanced Very High Resolution Radiometer daily quarter-degree, optimally interpolated product is freely available at NOAA-NCDC (http://eclipse.ncdc.noaa.gov/pub/OI-daily-v2/). The authors acknowledge Coriolis project for making publicly available in situ sea surface salinity data at http://www.coriolis.eu.org. The authors specially thank E. Mason for useful comments and for making *py-eddy-tracker* code freely available under a GNU license (http://www.imedea.uib.es/users/emason/py-eddy-tracker).

References

Bonjean, F., and G. S. E. Lagerloef (2002), Diagnostic model and analysis of the surface currents in the tropical pacific ocean, *J. Phys. Oceanogr.*, *32*(10), 2938–2954, doi:10.1175/1520-0485(2002)032<2938:DMAAOT>2.0.CO;2.

Boutin, J., N. Martin, G. Reverdin, X. Yin, and F. Gaillard (2012), Sea surface freshening inferred from SMOS and Argo salinity: Impact of rain, *Ocean Sci. Discuss.*, *9*(5), 3331–3357, doi:10.5194/osd-9-3331-2012.

Chelton, D. B., P. Gaube, M. G. Schlax, J. J. Early, and R. M. Samelson (2011), The influence of nonlinear mesoscale eddies on near-surface oceanic chlorophyll, *Science*, *334*(6054), 328–332, doi:10.1126/science.1208897.

Cornillon, P., T. Lee, and G. Fall (1994), On the probability that a gulf stream meander crest detaches to form a warm core ring, *J. Phys. Oceanogr.*, *24*(1), 159–171, doi:10.1175/1520-0485(1994)024<0159:OTPTAG>2.0.CO;2.

Csanady, G. T. (1979), The birth and death of a warm core ring, *J. Geophys. Res.*, *84*(C2), 777–780, doi:10.1029/JC084iC02p00777.

Daganzo-Eusebio, E., R. Oliva, Y. Kerr, S. Nieto, P. Richaume, and S. Mecklenburg (2013), SMOS radiometer in the 14001427-MHz passive band: Impact of the RFI environment and approach to its mitigation and cancellation, *IEEE Trans. Geosci. Remote Sens.*, *51*(10), 4999–5007, doi:10.1109/TGRS.2013.2259179.

Dewar, W. K. (1986), Mixed layers in gulf stream rings, *Dyn. Atmos. Oceans*, *10*(1), 1–29, doi:10.1016/0377-0265(86)90007-2.

Evans, R. H., K. S. Baker, O. B. Brown, and R. C. Smith (1985), Chronology of warm-core ring 82B, *J. Geophys. Res.*, *90*(C5), 8803–8811, doi:10.1029/JC090iC05p08803.

Frisch, U. (1995), *Turbulence: The Legacy of A. N. Kolmogorov*, Cambridge Univ. Press, Cambridge, U. K.

Fuglister, F. (1977), A cyclonic ring formed by the Gulf Stream, 1967, in *A Voyage of Discovery: George Deacon 70th Anniversary Volume, Supp. to Deep-Sea Research*, edited by M. V. Angel, pp. 177–192, Pergamon, Oxford, U. K.

Gierach, M. M., J. Vazquez-Cuervo, T. Lee, and V. M. Tsontos (2013), Aquarius and SMOS detect effects of an extreme Mississippi River flooding event in the Gulf of Mexico, *Geophys. Res. Lett.*, *40*, 5188–5193, doi:10.1002/grl.50995.

Grodsky, S. A., N. Reul, G. Lagerloef, G. Reverdin, J. A. Carton, B. Chapron, Y. Quilfen, V. N. Kudryavtsev, and H.-Y. Kao (2012), Haline hurricane wake in the Amazon/Orinoco plume: AQUARIUS/SACD and SMOS observations, *Geophys. Res. Lett.*, *39*, L20603, doi:10.1029/2012GL053335.

Hausmann, U., and A. Czaja (2012), The observed signature of mesoscale eddies in sea surface temperature and the associated heat transport, *Deep Sea Res., Part I*, *70*, 60–72, doi:10.1016/j.dsr.2012.08.005.

Isern-Fontanet, J., A. Turiel, E. Garcia-Ladona, and J. Font (2007), Microcanonical multifractal formalism: Application to the estimation of ocean surface velocities, *J. Geophys. Res.*, *112*, C05024, doi:10.1029/2006JC003878.

Kelly, K. A., R. J. Small, R. M. Samelson, Q. Bo, T. M. Joyce, K. Young-Oh, and M. F. Cronin (2010), Western boundary currents and frontal air-sea interaction: Gulf Stream and Kuroshio Extension, *J. Clim.*, *23*(21), 5644–5667, doi:10.1175/2010JCLI3346.1.

Lee, C. M., and K. H. Brink (2010), Observations of storm-induced mixing and Gulf Stream Ring incursion over the southern flank of Georges Bank: Winter and summer 1997, *J. Geophys. Res.*, *115*, C08008, doi:10.1029/2009JC005706.

Leterme, S. C., and R. D. Pingree (2008), The Gulf Stream, rings and North Atlantic eddy structures from remote sensing (Altimeter and SeaWiFS), *J. Mar. Syst.*, *69*(34), 177–190, doi:10.1016/j.jmarsys.2005.11.022.

Lewis, E. (1980), The practical salinity scale 1978 and its antecedents, *IEEE J. Oceanic Eng.*, *5*(1), 3–8.

Lovejoy, S., D. Schertzer, Y. Tessier, and H. Gaonac'h (2001), Multifractals and resolution-independent remote sensing algorithms: The example of ocean colour, *Int. J. Remote Sens.*, *22*(7), 1191–1234, doi:10.1080/01431160151144314.

Mason, E., A. Pascual, and J. C. McWilliams (2014), A new sea surface height–based code for oceanic mesoscale eddy tracking, *J. Atmos. Oceanic Technol.*, *31*(5), 1181–1188.

Nieves, V., C. Llebot, A. Turiel, J. Solé, E. García-Ladona, M. Estrada, and D. Blasco (2007), Common turbulent signature in sea surface temperature and chlorophyll maps, *Geophys. Res. Lett.*, *34*, L23602, doi:10.1029/2007GL030823.

Parisi, G., and U. Frisch (1985), On the singularity structure of fully developed turbulence, in *Turbulence and Predictability in Geophysical Fluid Dynamics, Proc. Intl. School of Physics E. Fermi*, edited by M. Ghil, R. Benzi, and G. Parisi, pp. 84–87, North Holland, Amsterdam.

Parker, C. E. (1971), Gulf stream rings in the sargasso sea, *Deep Sea Res. Oceanogr. Abstr.*, *18*(10), 981–993, doi:10.1016/0011-7471(71)90003-9.

Pingree, R. D., P. M. Holligan, and G. T. Mardell (1979), Phytoplankton growth and cyclonic eddies, *Nature*, *278*(5701), 245–247, doi:10.1038/278245a0.

Pont, O., A. Turiel, and C. Pérez-Vicente (2009), Empirical evidences of a common multifractal signature in economic, biological and physical systems, *Physica A*, *388*, 2025–2035, doi:10.1016/j.physa.2009.01.041.

Press, W. H., B. P. Flannery, S. Teukolsky, and W. T. Vetterling (1986), *Numerical Recipes, the Art of Scientific Computing*. Cambridge University Press, Cambridge, U. K.

Reul, N., and CATDS-CECOS Team (2012), SMOS Level 3 SSS research products—product user manual—Reprocessed years 2010–2012, technical report, IFREMER-CATDS-CECOS-L3-PUDOC, Laboratoire d'Océanographie Pysique et Spatiale, Plouzané, France.

Reul, N., J. Tenerelli, B. Chapron, D. Vandemark, Y. Quilfen, and Y. Kerr (2012), SMOS satellite L-band radiometer: A new capability for ocean surface remote sensing in hurricanes, *J. Geophys. Res.*, *117*, C02006, doi:10.1029/2011JC007474.

Reul, N., et al. (2014), Sea surface salinity observations from space with the SMOS satellite: A new means to monitor the marine branch of the water cycle, *Surv. Geophys.*, *35*(3), 681–722, doi:10.1007/s10712-013-9244-0.

Reynolds, R. W., T. M. Smith, C. Liu, D. B. Chelton, K. S. Casey, and M. G. Schlax (2007), Daily high-resolution-blended analyses for sea surface temperature, *J. Clim.*, *20*(22), 5473–5496, doi:10.1175/2007JCLI1824.1.

Richardson, P. (1983), Gulf stream rings, in *Eddies in Marine Science*, edited by A. Robinson, Springer, Berlin, pp. 19–45, doi:10.1007/978-3-642-69003-7.

Saunders, P. (1971), Anticyclonic eddies formed from shoreward meanders of the Gulf Stream, *Deep Sea Res. Oceanogr. Abstr.*, *18*(12), 1207–1219, doi:10.1016/0011-7471(71)90027-1.

Savidge, D. K. (2004), Gulf stream meander propagation past Cape Hatteras, *J. Phys. Oceanogr.*, *34*(9), 2073–2085.

The Ring Group (1981), Gulf stream cold-core rings: Their physics, chemistry, and biology, *Science*, *212*(4499), 1091–1100, doi:10.1126/science.212.4499.1091.

Tomczak, M., and J. S. Godfrey (2003), *Regional Oceanography: An Introduction*, Daya Books, New Delhi, India.

Turiel, A., and N. Parga (2000), Multifractal wavelet filter of natural images, *Phys. Rev. Lett.*, *85*, 3325–3328.

Turiel, A., and C. Pérez-Vicente (2005), Role of multifractal sources in the analysis of stock market time series, *Physica A*, *355*, 475–496.

Turiel, A., J. Grazzini, and H. Yahia (2005), Multiscale techniques for the detection of precipitation using thermal IR satellite images, *IEEE Geosci. Remote Sens. Lett.*, *2*(4), 447–450, doi:10.1109/LGRS.2005.852712.

Turiel, A., C. Pérez-Vicente, and J. Grazzini (2006), Numerical methods for the estimation of multifractal singularity spectra on sampled data: A comparative study, *J. Comput. Phys.*, *216*(1), 362–390.

Turiel, A., H. Yahia, and C. Pérez-Vicente (2008a), Microcanonical multifractal formalism: A geometrical approach to multifractal systems. Part I: Singularity analysis, *J. Phys. A*, *41*, 015501, doi:10.1088/1751-8113/41/1/015501.

Turiel, A., J. Solé, V. Nieves, J. Ballabrera-Poy, and E. García-Ladona (2008b), Tracking oceanic currents by singularity analysis of Microwave Sea Surface Temperature images, *Remote Sens. Environ.*, *112*, 2246–2260, doi:10.1016/j.rse.2007.10.007.

Turiel, A., V. Nieves, E. García-Ladona, J. Font, M.-H. Rio, and G. Larnicol (2009), The multifractal structure of satellite temperature images can be used to obtain global maps of ocean currents, *Ocean Sci.*, *5*, 447–460.

Turiel, A., et al. (2014), Sensibility to noise of new multifractal fusion methods for ocean variables, *Nonlinear Process. Geophys.*, *21*, 291–301.

Umbert, M., N. Hoareau, A. Turiel, and J. Ballabrera-Poy (2014), New blending algorithm to synergize ocean variables: The case of SMOS sea surface salinity maps, *Remote Sens. Environ.*, *146*, 172–187, doi:10.1016/j.rse.2013.09.018.

Zine, S., J. Boutin, P. Waldteufel, J. L. Vergely, T. Pellarin, and P. Lazure (2007), Issues about retrieving sea surface salinity in coastal areas from SMOS data, *IEEE Trans. Geosci. Remote Sens.*, *45*(7), 2061–2072, doi:10.1109/TGRS.2007.894934.